Reactive transport LBM model for CO$_2$ injection in fractured reservoirs

Zhiwei Tian [a,b,*], Huilin Xing [c], Yunliang Tan [d], Sai Gu [e], Suzanne D. Golding [c]

[a] State Key Laboratory of Coal Mine Disaster Dynamics and Control, Chongqing University, Chongqing 400030, China
[b] Faculty of Earth Resources, China University of Geosciences (Wuhan), Wuhan 430074, China
[c] School of Earth Sciences, The University of Queensland, Brisbane, QLD 4072, Australia
[d] State Key Laboratory of Mining Disaster Prevention and Control Co-founded by Shandong Province and the Ministry of Science and Technology, Shandong University of Science and Technology, Qingdao 266590, China
[e] School of Energy, Environment and Agrifood, Cranfield University, Cranfield, Bedfordshire MK43 0AL, UK

ARTICLE INFO

ABSTRACT

A geochemical LBM model has been developed to simulate the CO$_2$ injection in homogeneous porous media in our previous work. That model has the ability to investigate the coupled reactive transport processes with reactants and products ions transport, matrix dissolution, and dissolution induced porosity change. In the present work, the model is extended to study the reactive transport properties in "fractured" media. Two kinds of fractures are investigated: one is straightforward along the centerline, and the other is inclined. The reaction rate distribution and evolution are analyzed at different time steps. The dissolution property of fracture edges is also studied, the bottom edge dissolution rate is generally higher than that of the upper edge in inclined fractured media. The porosity change becomes more and more obvious with the increase of time steps, as well as the edge porosity profiles. For the different fracture width, the dissolution rate and edge porosity become higher with the increase of fracture width. All the results show that the present model has the capability to numerically investigate CO$_2$ injection and reactive transport in fractured reservoirs.

1. Introduction

CO$_2$ geological sequestration in deep saline aquifers, depleted oil and gas reservoirs, or unminable coal seams has been considered as an important strategy to reduce CO$_2$ emission into the atmosphere (IPCC, 2005). The whole system of CO$_2$ geological sequestration is a highly coupled process including geochemical reactive transport, fluid flow, and complex interactions (Gaus et al., 2008; Gaus, 2010).

When the CO$_2$–water is injected into a reservoir, the main involved processes are the transport, chemical and mechanical processes and their interactions (Li et al., 2009, 2006; Wei et al., 2015). Recent numerical models for CO$_2$ geological sequestration applications can be divided into three categories (Gaus et al., 2008): (1) hydrodynamic model, (2) batch geochemical model, and (3) reactive transport model. Obviously, reactive transport model is the most realistic, but the most challenging one to perform (Gaus et al., 2008, 2004; Gaus, 2010; Li et al., 2007; Li, 2011).

The lattice Boltzmann method (LBM) has made rapid progress since its appearance (Chen and Doolen, 1998; Succi, 2001; Sukop and Thorne, 2007; Llewellin, 2010a, b), and also been widely applied in many fields (Sukop and Thorne, 2007; Coon et al., 2014; Chen and Tian, 2009, 2010; Tian et al., 2006, 2007, 2010, 2012; Gao et al., 2014), including fluid flow in porous media therein. Kang et al. (2002a) developed a pore-scale LBM model for fluid flow and chemical reaction in porous media. A multi-component model was then presented for simulating reactive transport between the multiple species and minerals (Kang et al., 2006), and applied in simulating the injection processes of CO$_2$–water into reservoirs in CO$_2$ geological sequestration (Kang et al., 2010). Recently, Kang et al. (2014) numerically studied the dissolution-induced changes in permeability and porosity at the pore scale.

However, the pore-scale model needs detailed geometric information, and the computational domain size is limited to a relatively small scale and thus not suitable for practical field applications (Guo and Zhao, 2002). An alternative approach is widely used at the representative elementary volume (REV) scale (Kang et al., 2002b). In classical studies, fluid flow in porous media is usually modeled by some semi-empirical models based on the volume-averaging at the REV scale, such as the Darcy model. The great advantage of REV models is that the complex microscopic

* Corresponding author at: Faculty of Earth Resources, China University of Geosciences (Wuhan), Wuhan 430074, China.
E-mail address: zwtian@cug.edu.cn (Z. Tian).

structure of the porous medium can be ignored, and its main statistical properties are directly included to describe flow patterns.

In our previous work (Tian et al., 2014), geochemical reaction LBM model has been developed to investigate the coupled processes of fluid flow, solid phase dissolution and species reactive transport in homogeneous porous media. The dissolution-induced porosity changes and its feedback impacts on flow field can be also numerically analyzed. By extending our former model, CO_2 injection in *fractured* reservoir with reactive transport is numerically investigated in this study.

The remaining parts are organized as follows: Section 2 revisits the generalized LBM model for porous flows, and particularly points out the treatment for fractured porous media. In Section 3, the geochemical reaction model is introduced, including species transport, dissolution reaction, porosity and permeability change. The reactive transport features in fractured media are illustrated in detail in Section 4 with some discussions, and the last section summarizes the whole paper.

2. Lattice Boltzmann model for porous flows

Guo and Zhao (2002) proposed a generalized LBM model for simulating fluid flow in porous media at the REV scale, by introducing the porosity and adding the force terms.

2.1. Generalized equations for porous flows

The generalized Navier–Stokes (N–S) equations to describe the fluid flow in porous media are

$$\nabla \cdot \mathbf{u} = 0 \tag{1}$$

$$\frac{\partial \mathbf{u}}{\partial t} + \frac{1}{\epsilon}(\mathbf{u} \cdot \nabla)\mathbf{u} = -\frac{1}{\rho}\nabla(\epsilon p) + \nu_e \nabla^2 \mathbf{u} + \mathbf{F} \tag{2}$$

here $\mathbf{u}$, ρ and p are the fluid velocity, density and pressure, respectively. ϵ is the porosity, $\nu_e = \nu \cdot J\epsilon$ is the effective viscosity, and $\mathbf{F}$ stands for the total body force given by

$$\mathbf{F} = -\frac{\epsilon\nu}{K}\mathbf{u} - \frac{\epsilon F_\epsilon}{\sqrt{K}}|\mathbf{u}|\mathbf{u} + \epsilon\mathbf{G} \tag{3}$$

here ν is the kinematic viscosity of the fluid, and $\mathbf{G}$ is the external body force. The geometric function F_ϵ and the permeability K of porous media are related to the porosity, and can be expressed as (Carman, 1956)

$$F_\epsilon = \frac{1.75}{\sqrt{150\epsilon^3}} \tag{4}$$

$$K = \frac{\epsilon^3 d_p^2}{150(1-\epsilon)^2} \tag{5}$$

here d_p is the solid particle diameter.

As known, there is no "universal" porosity–permeability relationship valid for all porous medium and the Kozeny–Carman equation (Eq. (5)) is the widely used one, although it is originally derived from sphere or grain packed media. Furthermore, this relationship expression in our model can be conveniently replaced by a more particular and realistic expression if necessary.

2.2. Porous LBM model

In the LBM model for porous media, the evolution equation of the particle distribution function f_i is as followed with the force term:

$$f_i(\mathbf{x} + \mathbf{c}_i\Delta t, t + \Delta t) - f_i(\mathbf{x}, t) = -\frac{1}{\tau}\Big[f_i(\mathbf{x}, t) - f_i^{eq}(\mathbf{x}, t)\Big] + \Delta t F_i \tag{6}$$

here $\mathbf{x}$ and t represent the node position and time, $\mathbf{c}_i$ is the particle discrete velocity along the ith discrete direction. Δt and τ are the time step and relaxation time, respectively. The equilibrium distribution function f_i^{eq} and the force term F_i are given by

$$f_i^{eq} = \omega_i\rho\left[1 + \frac{\mathbf{c}_i\cdot\mathbf{u}}{c_s^2} + \frac{\mathbf{uu}:(\mathbf{c}_i\mathbf{c}_i - c_s^2\mathbf{I})}{2\epsilon c_s^4}\right] \tag{7}$$

$$F_i = \omega_i\rho\left(1 - \frac{1}{2\tau}\right)\left[\frac{\mathbf{c}_i\cdot\mathbf{F}}{c_s^2} + \frac{\mathbf{uF}:(\mathbf{c}_i\mathbf{c}_i - c_s^2\mathbf{I})}{\epsilon c_s^4}\right] \tag{8}$$

here the total body force $\mathbf{F}$ is obtained by Eq. (3). The porosity ϵ is included in both f_i^{eq} and F_i.

Accordingly, the density and the fluid velocity are defined as

$$\rho = \sum_i f_i, \quad \rho\mathbf{u} = \sum_i \mathbf{c}_i f_i + \frac{\Delta t}{2}\rho\mathbf{F} \tag{9}$$

Note that $\mathbf{F}$ also contains the velocity $\mathbf{u}$ (see Eq. (3)), the velocity can be given explicitly by

$$\mathbf{u} = \frac{\mathbf{v}}{c_0 + \sqrt{c_0^2 + c_1|\mathbf{v}|}} \tag{10}$$

here $\mathbf{v}$ is a temporal velocity defined as

$$\rho\mathbf{v} = \sum_i \mathbf{c}_i f_i + \frac{\Delta t}{2}\epsilon\rho\mathbf{G} \tag{11}$$

and the parameters c_0, c_1 are given by

$$c_0 = \frac{1}{2}\left(1 + \epsilon\frac{\Delta t}{2}\frac{\nu}{K}\right), \quad c_1 = \epsilon\frac{\Delta t}{2}\frac{F_\epsilon}{\sqrt{K}} \tag{12}$$

The pressure $p = \rho c_s^2/\epsilon$ and the effective viscosity $\nu_e = (\tau - 0.5)c_s^2\Delta t$. By using the Chapman–Enskog procedure, the generalized N–S equation Eq. (2)) can be recovered in the incompressible limit. More details can be referred to Guo and Zhao (2002).

2.3. Transport in fractured media

For reactive transport in fractured rocks, fluid flow and transport of species occur primarily through fractures, while species may infiltrate the matrix blocks through relatively slow diffusion. Methods developed for fluid flow in fractured rocks can be applied to geochemical transport (Xu and Preuss, 2001; Preuss and Narasimhan, 1985).

In the present porous LBM model, it is quite easy to describe the flow in fracture. In the absence of porous medium, we can take the porosity as

$$\epsilon \to 1.0 \tag{13}$$

And for the other part of the porous matrix, the porosity remains as the original value ϵ_0. With this simple and effective treatment, the generalized momentum equation (Eq. (2)) naturally reduces to the Navier–Stokes equation for free fluid flows. And the LBM evolution equation (Eq. (6)), the equilibrium distribution function (Eq. (7)), and the external force term (Eq. (8)) are also reduce to the standard LBM forms when $\epsilon \to 1.0$. Numerical validations has been carried out by Guo and Zhao (2002), and shows the good agreement between the numerical and analytical solutions. The present model can also capture the interface velocity

gradient without incorporating the stress boundary condition in simulations.

3. CO_2 geochemical LBM model

3.1. Equilibrium reaction and kinetic rate

In the process of CO_2 geological sequestration, although pure CO_2 is generally assumed to be very little reactive, once in contact with water/brine, it will form carbonic acid and thus leads to reactions as (Gaus et al., 2008, 2004; Gaus, 2010; Yin et al., 2012):

$$CO_2 + H_2O \rightleftharpoons H_2CO_3 \rightleftharpoons H^+ + HCO_3^- \qquad (14)$$
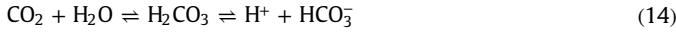
carbonic acid is a kind of weak acid that will cause a drop in the brine's pH and an "acid attack" on the host rock.

For simply, we assume that the main reactant mineral is pure $CaCO_3$, which builds up the solid matrix of the host rock. Nevertheless, our model can be further extended by adding multiple minerals with certain reactions. The simplified overall reaction with the CO_2–water can be described as

$$CaCO_3 + H^+ \rightleftharpoons Ca^{++} + HCO_3^- \qquad (15)$$

When modeling geochemical reactions for CO_2 geological sequestration process, reaction kinetics generally need to be included in order to obtain a reliable outcome. Many kinetic laws are described in the literature (Plummer et al., 1978; Chou et al., 1989; Pokrovsky et al., 2005, 2009; Spycher et al., 2003). The most popular one used in geochemical reaction modeling applied can be expressed as

$$R = \left(k_1 a_{H^+} + k_2 a_{H_2CO_3^*} + k_3 \right)\left(1 - \frac{Q}{K_{eq}} \right) \qquad (16)$$

here k_i are the reaction rate constants, a_{H^+} and $a_{H_2CO_3^*}$ refer to the activities of H^+ and $H_2CO_3^*$, respectively. K_{eq} is the equilibrium constant, and Q is the ion activity product (IAP) that relates to the concentrations of Ca^{++} and HCO_3^-.

3.2. Reaction species model

Now, we focus on how to compute the species (or ions) distribution in the LBM frame with chemical reaction.

The evolution equations for different species with reaction are

$$g_{Y_{j,i}}(\mathbf{x} + \mathbf{c}_i \Delta t, t + \Delta t) - g_{Y_{j,i}}(\mathbf{x}, t)$$
$$= -\frac{1}{\tau_j}\left[g_{Y_{j,i}}(\mathbf{x}, t) - g_{Y_{j,i}}^{eq}(\mathbf{x}, t) \right] + \omega_i R_s \Delta t \qquad (17)$$

where $g_{Y_{j,i}}$ is the ith distribution function for the jth species, τ_j is the dimensionless relaxation time for the jth species, and R_s is the species reaction source term which is correlated with the kinetic reaction rate mentioned in the last subsection. $g_{Y_{j,i}}^{eq}$ is the equilibrium distribution function for the jth species:

$$g_{Y_{j,i}}^{eq} = \omega_i Y_j \left[1 + \frac{(\mathbf{c}_i \cdot \mathbf{u})}{c_s^2} + \frac{(\mathbf{c}_i \cdot \mathbf{u})^2}{2c_s^4} - \frac{|\mathbf{u}|^2}{2c_s^2} \right] \qquad (18)$$

Y_j represents the jth species concentration in the bulk fluid.

The species concentration Y_j can be addressed in terms of the distribution function:

$$Y_j = \sum_i g_{Y_{j,i}} \qquad (19)$$

and the jth species diffusion coefficient D_j can be given by

$$D_j = (\tau_{Y_j} - 0.5)c_s^2 \Delta t \qquad (20)$$

All the species concentration in Eq. (15) can be achieved from the above, except the solid phase $CaCO_3$. In the next, we will discuss dealing with the calcium carbonate reaction and its link with porosity and permeability change.

3.3. Solid phase reaction and porosity change

A reaction rate equation of solid phase mass Y_c of calcium carbonate $CaCO_3$ is (Parkhurst and Appelo, 1999; Yin et al., 2012)

$$\frac{\partial Y_c}{\partial t} = M_c R_c \qquad (21)$$

here M_c is the $CaCO_3$ molecular weight, and R_c is the overall reaction rate at the present grid.

With the reaction dissolution of solid phase $CaCO_3$, the volume of the solid matrix becomes less and the porosity increases. Thereby, the porosity is obtained by

$$\epsilon = 1.0 - (1.0 - \epsilon_0)\frac{Y_c}{Y_{c0}} \qquad (22)$$

the porosity of every grid will be updated after each time step. In our simulation, the initial porosity ϵ_0 is 0.1, and Y_c/Y_{c0} is the mass fraction.

In the following step, based on Kozeny–Carman equation Eq. (5)), the permeability changes are calculated from the porosity at each time step as

$$K = K_0 \left(\frac{\epsilon}{\epsilon_0} \right)^3 \left(\frac{1 - \epsilon_0}{1 - \epsilon} \right)^2 \qquad (23)$$

This permeability and porosity change subsequently impacts the flow properties through the force term definition (Eq. (3)), LBM evolution equation Eq. (6)) and macro variables statistics (Eq. (9)). Therefore, our model has the capability of describing the coupled processes of solute reaction transport, solid matrix dissolution, porosity and permeability change, and velocity increase.

4. Simulation results and discussion

In this section, numerical simulations are carried out by using the developed model. We assume that in the injection of CO_2 saturated water into a carbonate aquifer from the left inlet to the right. The computational grids adopted herein are 201×201. The initial matrix porosity is 10%, and the fracture is straightly along the centerline or along a 45° inclined line (Fig. 1). The initial concentration of H^+ at the inlet is set as 1.0×10^{-4} (mol/L), while those of Ca^{++} and HCO_3^- are both 0.0. The geochemical parameters used in Eq. (16) are from the typical experimental data in Chou et al. (1989) and Plummer et al. (1978). Since the dissolution rate of calcium carbonate is quite low, the $CaCO_3$ matrix will not be totally dissolved in our simulations.

4.1. Centerline fractured reactive transport

With the injection of CO_2–water, the matrix is dissolved due to the acid attack. In the first case, the fracture width is $H/10$. Due to the existing of fracture, the dissolution occurs not only near the inlet but also along the fracture edges. This can be illustrated from the contour of nondimensional reaction rate (Figs. 2 and 3 at 10,000 and 5×10^5 time steps, respectively). The entrance region keeps the most intense reaction and then dissolution rate rapidly drops in the downstream matrix. While along the fracture edges, the reaction rate drops gradually. This is mainly caused by the
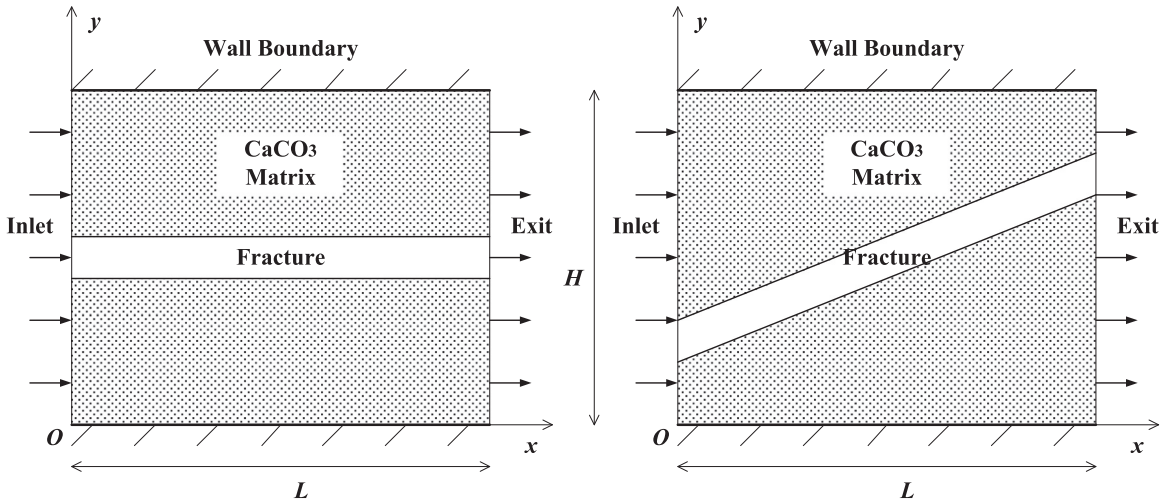
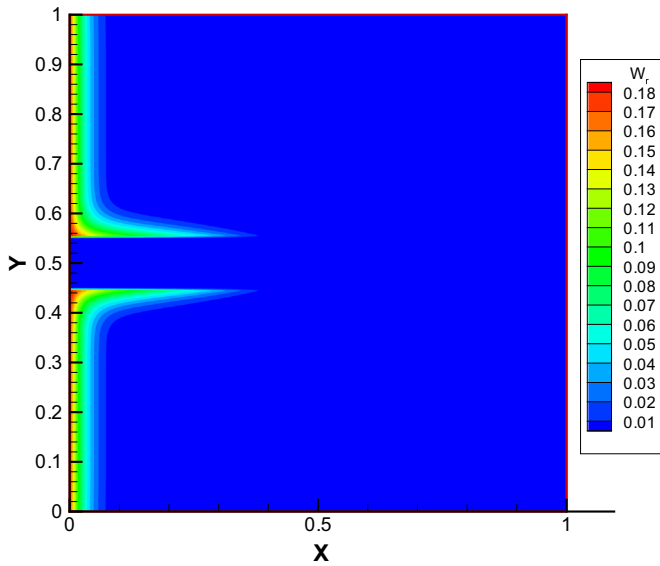Fig. 1. Sketch of the computational domain with fractures in different directions.

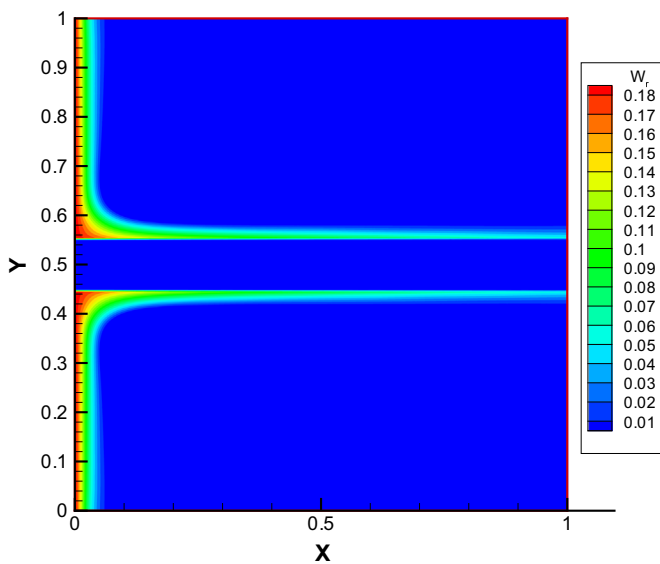Fig. 2. Contours of nondimensional reaction rate at 10,000 time steps.

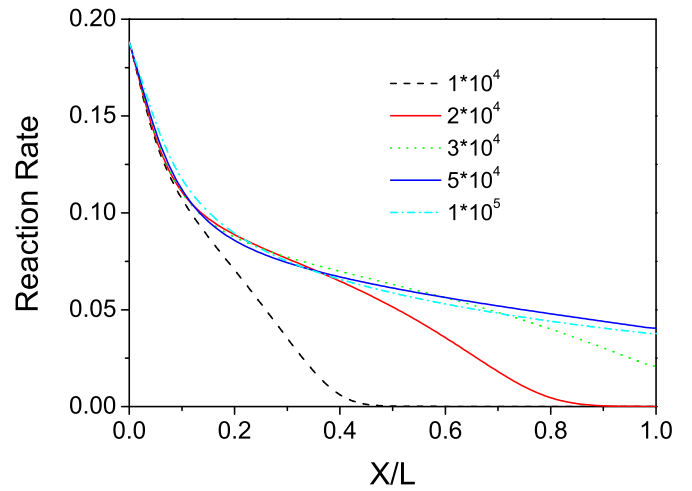Fig. 3. Contours of nondimensional reaction rate at 5×10^5 time steps.

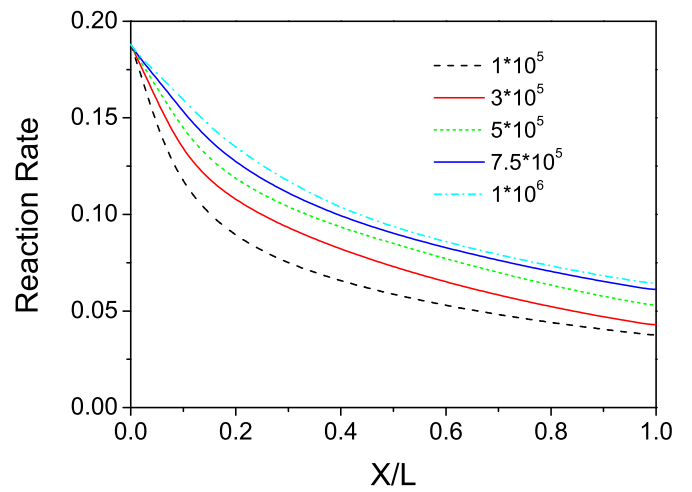Fig. 4. Fracture edge dissolution rate at different time steps (till 1×10^5).

Fig. 5. Fracture edge dissolution rate at different time steps (from 1×10^5 to 1×10^6).

different flow and transport pattern in fracture. Figs. 4 and 5 show the edge dissolution rate at different time steps, from the beginning to 1×10^6 time steps. At the early stage of injection, the downstream edge is not dissolved where the reactant has not reached. The reaction front move forwards along with the
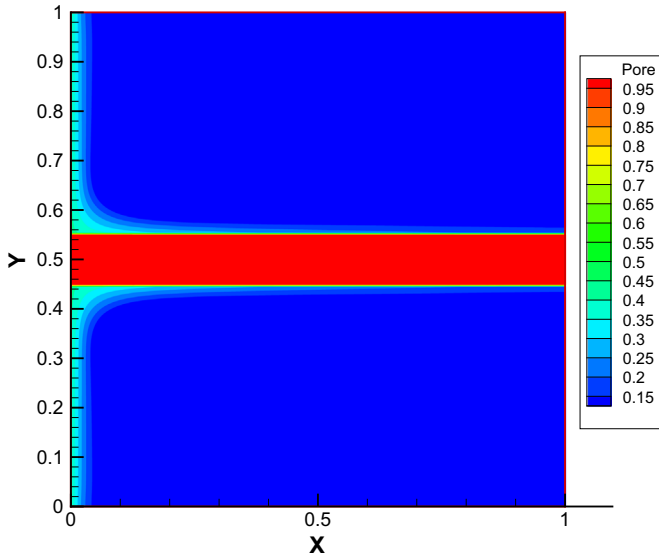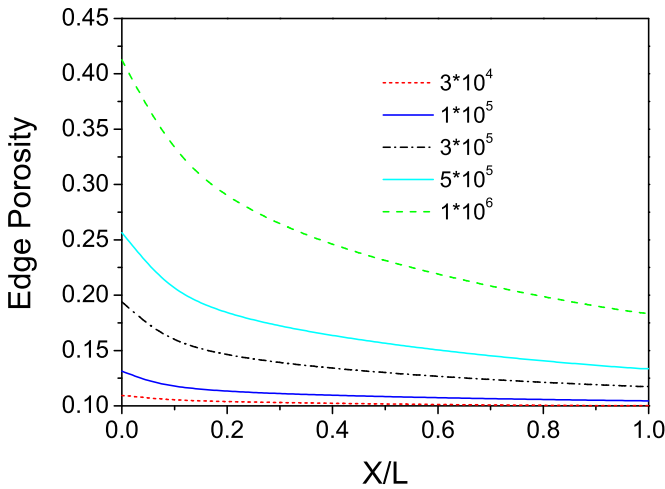
Fig. 6. Porosity distribution at 1×10^6 time steps.

Fig. 7. Edge porosity profiles at different time steps.

Fig. 8. Edge dissolution rate for different fracture width at 5×10^5 time steps.

Fig. 9. Edge porosity profiles for different fracture width at 5×10^5 time teps.

Fig. 10. Contours of nondimensional reaction rate in sloped fracture at 1×10^4 time steps.

injection process and the whole edge start to be dissolved at around 30,000 time steps. After that, the fracture edge dissolution rate keeps going upwards till reaching a stable state.

With the dissolution of matrix, the porosity changes. The porosity contour at 1×10^6 time steps is shown in Fig. 6. The porosity increase mostly appears at the inlet region because of the high concentration of reactant in that area. This observation is consistently relevant with the distribution of dissolution rate. Similarly, porosity change also happens along the fracture edge. The edge porosity change is not very distinct before 1×10^5 time steps. While the edge porosity distribution curves go up with the time steps in Fig. 7. And the inlet edge porosity can reach 41.3% at 1×10^6 time steps, as well as 18.4% at outlet.

Moreover, the numerical investigation with different fracture width is also carried out for comparison. The edge dissolution rate at 5×10^5 time steps are compared in Fig. 8. When fracture width is $H/20$, the reactant reactive transport is limited and the edge dissolution can only be observed before $0.5L$. The dissolution rate is almost zero for the downstream edge. While for the fracture width of $H/6$, the edge dissolution becomes more intensive. The reaction rate is higher than that of $H/10$ width in the whole region. The edge porosity distribution shows the similar pattern in Fig. 9.
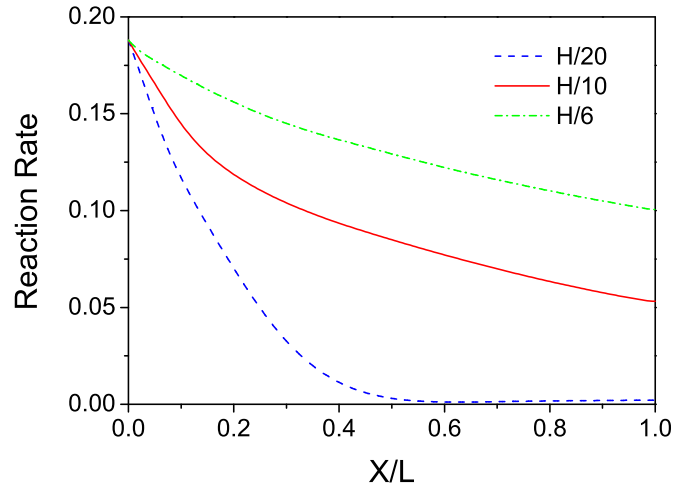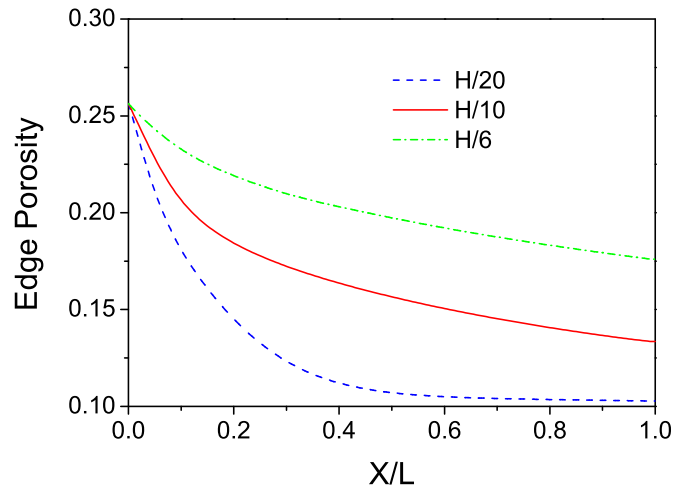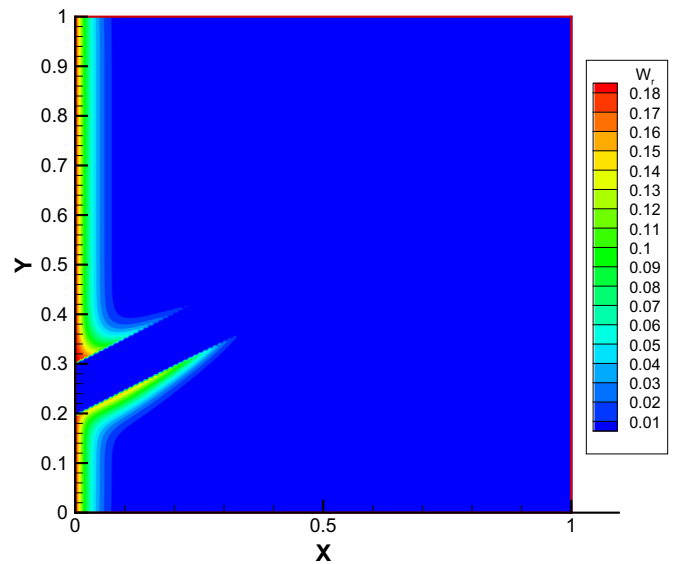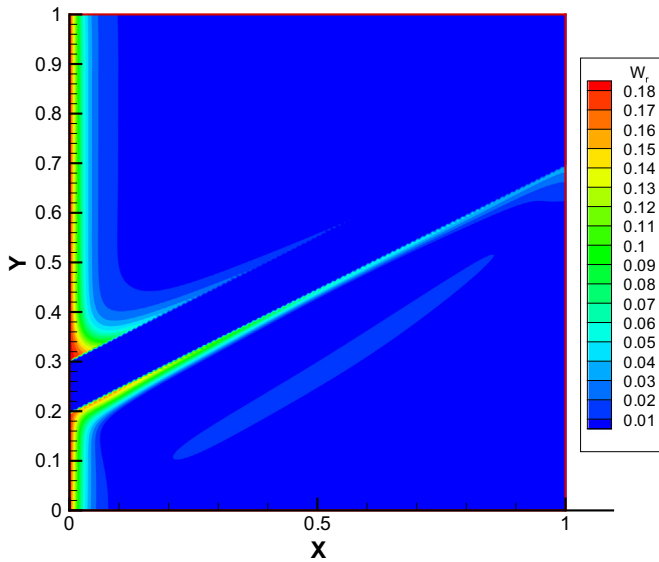
Fig. 11. Contours of nondimensional reaction rate in sloped fracture at 1×10^5 time steps.

The inlet porosity is almost the same for different width. The wider the fracture is, the more the edge porosity change can be observed.

4.2. Inclined fractured reactive transport

When the fracture is inclined with the streamline, the reactive transport property becomes different. Figs. 10, 11 and 12 show the reaction rate contours at 1×10^4, 1×10^5 and 1×10^6 time steps, respectively. At the beginning, the dissolution occurs only at limited entrance region, as well as the fracture edges (Fig. 10). With the injection and reactants transport, the fracture edge dissolution becomes more dramatically. Particularly, the dissolution of bottom fracture edge keeps non-zero till the outlet at 1×10^5 time steps (Fig. 13). After that, the dissolution rate distribution at bottom edge draws back upstream, mainly because that the downstream region behind the bottom edge gradually tends to be a equilibrium state. It is noted that in Fig. 13, the bottom edge dissolution rate of
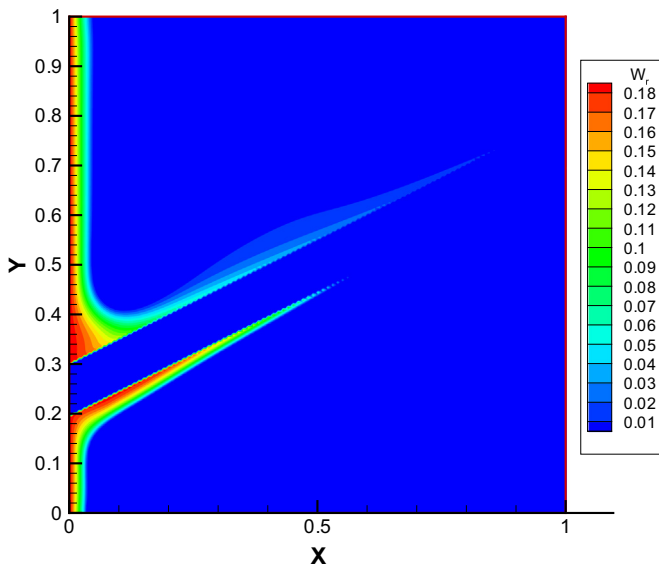

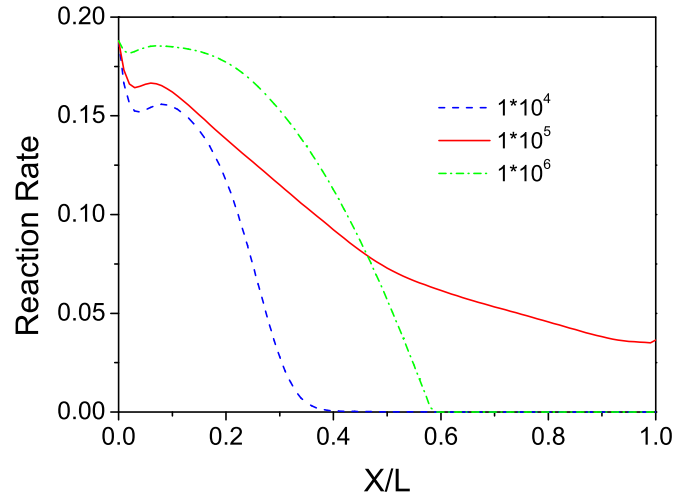**Fig. 12.** Contours of nondimensional reaction rate in sloped fracture at 1×10^6 time steps.

Fig. 13. Reaction rate profiles of bottom edge at different time steps.
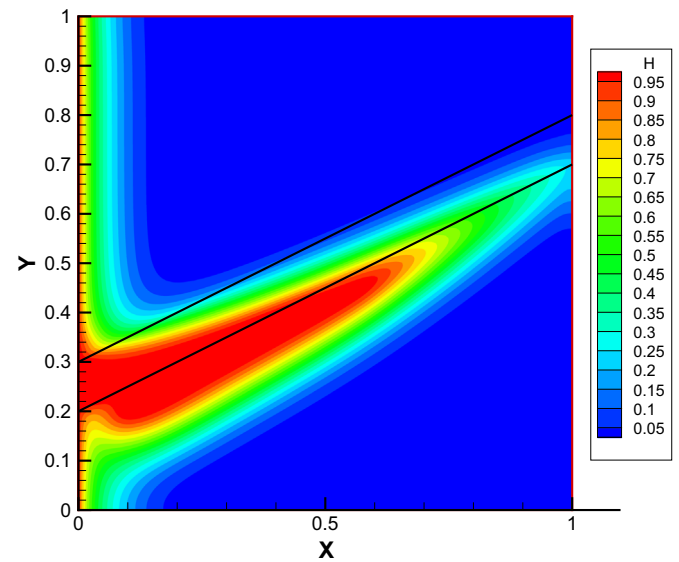

Fig. 14. Contours of H+ concentration in sloped fracture at 1×10^5 time steps.

upstream region ($X \leq 0.5L$) keeps going up with the time steps. This can also illustrated from the H^+ concentration distribution (Fig. 14). H^+ ions can easily transport along the fracture and into the matrix behind the bottom edge due to the horizontal driven forces.

In contrast, the upper edge dissolution rate becomes more sharp and prolongates longer downstream with the increase of time steps (Figs. 10–12). The dissolution rate of upper and bottom fracture edge is shown in Fig. 15. For the upper edge, the dissolution rate drops sharply before $X = 0.2L$ approximately, and then goes down gradually till the outlet. The reaction rate along the whole upper edge is non-zero. While for the bottom edge, the dissolution rate keeps at a relatively high level before $X = 0.3L$. In this upstream area, the bottom edge dissolution rate always keeps higher than that of the upper edge. And then, the dissolution rate falls dramatically to zero around $X = 0.6L$, where the edge dissolution reached to a equilibrium state. Therefore, in the downstream region, the upper edge dissolution rate can be higher after the dissolution reaction becoming equilibrium.

Fig. 16 shows the porosity contour at 1×10^6 time steps. Similarly to the Fig. 6, the porosity increase mainly appears in the entrance region and along fracture edges. However, the porosity distribution of upper and bottom edge performs differently since
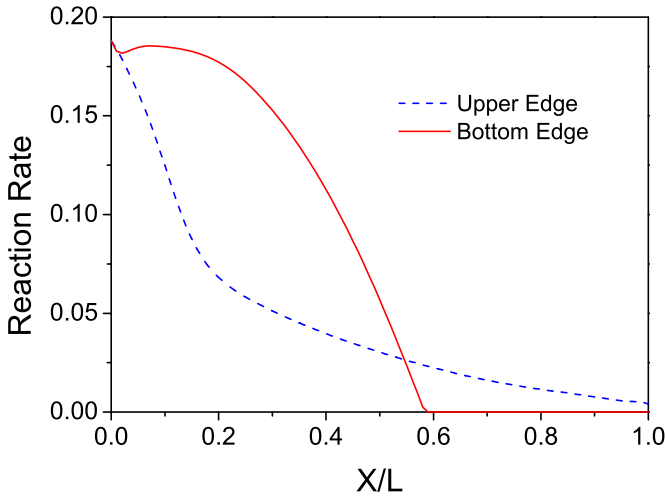
Fig. 15. Reaction rate profiles of upper and bottom edge at 1×10^6 time steps.
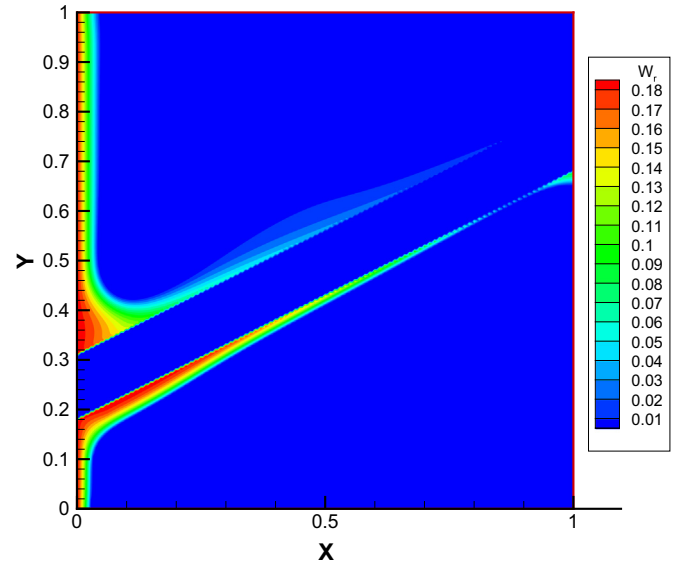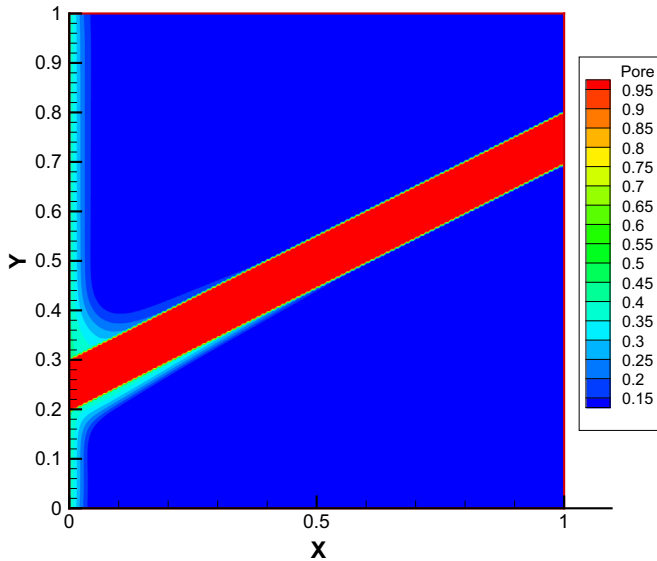

Fig. 16. Porosity distribution with sloped fracture at 1×10^6 time steps.

Fig. 17. Contours of nondimensional reaction rate at 1×10^6 time steps, fracture width is H/20.
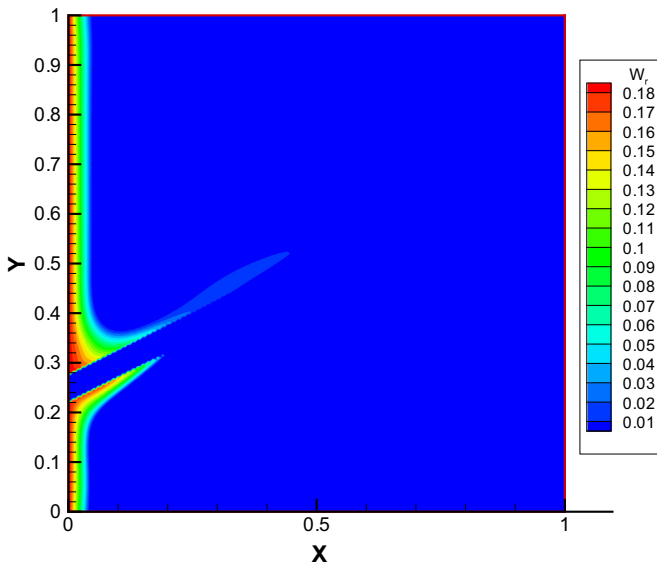

Fig. 18. Contours of nondimensional reaction rate at 1×10^6 time steps, fracture width is H/8.

the fracture is inclined. In the region between the entrance and upper edge, the porosity change is obvious and wider. While near the bottom edge, the domain of porosity increase is narrower but extends longer downstream (Fig. 16).

For different sloped fracture width, the reactive transport property can be compared by the reaction rate distribution (Figs. 17 and 18). When the inclined fracture width is H/20 (narrower than the previous case), the dissolution is limited to a relatively narrow area accordingly. For example, the bottom edge dissolution rate drops to zero around $X = 0.2L$, which is about $0.6L$ when the fracture width is H/10. On the contrary, the dissolution reaction becomes more intense (Fig. 18). The reaction area is broader both for the entrance and along the fracture edges. The dissolution rate is non-zero for the whole bottom fracture edge. Therefore, the influence of sloped fracture width is similar to that of the straightforward fracture width.

5. Conclusions

In this study, we numerically investigate on CO_2 injection in fractured media by extending our previous geochemical LBM model. In the case of centerline fractured media, the fracture edge dissolution rate at different time steps are detailed plotted to study the edge dissolution evolution properties. The porosity change becomes more and more obvious with the injection process. The edge porosity profiles are also going up continually. While the fracture is sloped, the upper edge and the bottom edge show the different characteristics of dissolution distribution and evolution. Generally, the bottom edge dissolution rate is higher than that of the upper edge. But in some particular areas, it is a little lower. By studying the influence of different fracture width for both cases, it is found that the wider the fracture is, the more intense the dissolution reaction will take, as well as the increasing in edge porosity. Our model consequently shows the capability to simulate the geochemical reactive transport in fractured reservoirs.

Acknowledgements

References

Carman, P.C., 1956. Flow of Gases Through Porous Media. Academic, San Diego, CA.

Chen, S.Y., Doolen, G.D., 1998. Lattice Boltzmann method for fluid flows. Ann. Rev. Fluid Mech. 30, 329–364.

Chen, S., Tian, Z.W., 2009. Simulation of microchannel flow using the lattice Boltzmann method. Physica A 388, 4803–4810.

Chen, S., Tian, Z.W., 2010. Simulation of thermal micro-flow using lattice Boltzmann method with Langmuir slip model. Int. J. Heat Fluid Flow 31, 227–235.

Chou, L., Garrels, R.M., Wollast, R., 1989. Comparative study of the kinetics and mechanisms of dissolution of carbonate minerals. Chem. Geol. 78, 269–282.

Coon, E.T., Porter, M.L., Kang, Q., 2014. Taxila LBM: a parallel, modular lattice-Boltzmann framework for simulating pore-scale flow in porous media. Comput. Geosci. 18, 17–27.

Gaus, I., Audigane, P., Andre, L., Lions, J., Jacquemet, N., Durst, P., Czernichowski-Lauriol, I., Azaroual, M., 2008. Geochemical modelling and solute transport modelling for CO_2 storage, what to expect from it? Int. J. Greenh. Gas Control 2, 605–625.

Gaus, I., 2010. Role and impact of CO_2-rock interactions during CO_2 storage in sedimentary rocks. Int. J. Greenh. Gas Control 4, 73–89.

Gao, J.F., Xing, H.L., Tian, Z.W., Muhlhaus, H., 2014. Lattice Boltzmann modeling and evaluation of fluid flow in heterogeneous porous media involving multiple matrix constituents. Comput. Geosci. 62, 198–207.

Guo, Z.L., Zhao, T.S., 2002. Lattice Boltzmann model for incompressible flows through porous media. Phys. Rev. E 66, 036304(9).

IPCC, 2005. IPCC special report on carbon dioxide capture and storage. In: Metz, B., Davidson, O., deConinck, H.C., Loos, M., Meyer, L.A. (Eds.), Cambridge University Press, Cambridge/New York.

Kang, Q., Zhang, D., Chen, S., He, X., 2002a. Lattice Boltzmann simulation of chemical dissolution in porous media. Phys. Rev. E 65, 036318(8).

Kang, Q., Zhang, D., Chen, S., 2002b. Unified lattice Boltzmann method for flow in multiscale porous media. Phys. Rev. E 66, 056307(11).

Kang, Q., Lichtner, P.C., Zhang, D., 2006. Lattice Boltzmann pore-scale model for multicomponent reactive transport in porous media. J. Geophys. Res. 111, B05203(12).

Kang, Q., Lichtner, P.C., Viswanathan, H.S., Abdel-Fattah, A.I., 2010. Pore scale modeling of reactive transport involved in geologic CO_2 sequestration. Transp. Porous Med. 82, 197–213.

Kang, Q., Chen, L., Valocchi, A.J., Viswanathan, H., 2014. Pore-scale study of dissolution-induced changes in permeability and porosity of porous media. J. Hydrol. 517, 1049–1055.

Li, Q., Wu, Z.S., Bai, Y.L., Yin, X.C., Li, X.C., 2006. Thermo-hydro-mechanical modeling of CO_2 sequestration system around fault environment. Pure Appl. Geophys. 163, 2585–2593.

Li, Q., Wu, Z.S., Lei, X.L., Murakami, Y., Satoh, T., 2007. Experimental and numerical study on the fracture of rocks during injection of CO_2-saturated water. Environ. Geol. 51, 1157–1164.

Li, Q., Ito, K., Fu, B.H., Sato, I., Lei, X.L., Okuyama, S., Sasai, T., Wu, Z.S., Kazahaya, K., Shi, B., 2009. Coupling and fusion in modern geosciences. Data Sci. J. 8, S45–S50.

Li, Q., 2011. Coupled reactive transport model for heat and density driven flow in CO_2 storage in saline aquifers. J. Hazard., Toxic, Radioact. Waste 15, 251–258.

Llewellin, E.W., 2010a. LBflow: an extensible lattice Boltzmann framework for the simulation of geophysical flows. Part I. Theory and implementation. Comput. Geosci. 36, 115–122.

Llewellin, E.W., 2010b. LBflow: an extensible lattice Boltzmann framework for the simulation of geophysical flows. Part II. Usage and validation. Comput. Geosci. 36, 123–132.

Parkhurst, D.L., Appelo, C.A.J., 1999. Users guide to PHREEQC (Version 2)—A computer program for speciation, batchreaction, one-dimensional transport, and inverse geochemical calculations. U.S. Geological Survey Water-Resources Investigations Report, 99-4259.

Plummer, L.N., Parkhurst, D.L., Wigley, T.M.L., 1978. The kinetics of calcite dissolution in CO_2–water systems at 5–60 °C and 0.0–1.0 atm CO_2. Am. J. Sci. 278, 176–216.

Pokrovsky, O.S., Golubev, S.V., Schott, J., 2005. Dissolution kinetics of calcite, dolomite and magnesite at 25 °C and 0–50 atm pCO_2. Chem. Geol. 217, 239–255.

Pokrovsky, O.S., Golubev, S.V., Schott, J., Castillo, A., 2009. Calcite, dolomite and magnesite dissolution kinetics in aqueous solutions at acid to circumneutral pH, 25–150 °C and 1–55 atm pCO_2: new constraints on CO_2 sequestration in sedimentary basins. Chem. Geol. 265, 20–32.

Pruess, K., Narasimhan, T.N., 1985. A practical method for modeling fluid and heat flow in fractured porous media. SPE J. 25, 14–26.

Spycher, N., Pruess, K., Ennis-King, J., 2003. CO_2–H_2O mixtures in the geological sequestration of CO_2. I. Assessment and calculation of mutual solubilities from 12 to 100 °C and up to 600 bar. Geochim. Cosmochim. Acta 67, 3015–3031.

Succi, S., 2001. The Lattice Boltzmann Equation for Fluid Dynamics and Beyond. Oxford University Press, Oxford.

Sukop, M.C., Thorne, D.T., 2007. Lattice Boltzmann Modeling: An Introduction for Geoscientists and Engineers, 2nd edition. Springer, Berlin Heidelberg, New York.

Tian, Z.W., Zou, C., Liu, Z.H., Guo, Z.L., Liu, H.J., Zheng, C.G., 2006. Lattice Boltzmann method in simulation of thermal micro-flow with temperature jump. Int. J. Mod. Phys. C 17, 603–614.

Tian, Z.W., Zou, C., Liu, H.J., Guo, Z.L., Liu, Z.H., Zheng, C.G., 2007. Lattice Boltzmann scheme for simulating thermal micro-flow. Physica A 385, 59–68.

Tian, Z.W., Chen, S., Zheng, C.G., 2010. Lattice Boltzmann simulation of gaseous finite-Knudsen microflows. Int. J. Mod. Phys. C 21, 769–783.

Tian, Z.W., Tan, Y.L., Chen, S., 2012. A numerical study on premixed micro-combustion by lattice Boltzmann method. Int. J. Mod. Phys. C 23 1250037(13).

Tian, Z.W., Xing, H.L., Tan, Y.L., Gao, J.F., 2014. A coupled lattice Boltzmann model for simulating geochemical reaction transport in CO_2 injection. Physica A 403, 155–164.

Wei, X.C., Li, Q., Li, X.Y., Sun, Y.K., Liu, X.H., 2015. Uncertainty analysis of impact indicators for the integrity of combined caprock during CO_2 geosequestration. Eng. Geol. 196, 37–46.

Xu, T., Pruess, K., 2001. Modelling multiphase non-isothermal fluid flow and reactive geochemical transport in variably saturated fractured rocks. 1. Methodology. Am. J. Sci. 301, 16–33.

Yin, S., Dusseault, M.B., Rothenburg, L., 2012. Coupled THMC modeling of CO_2 injection by finite element methods. J. Pet. Sci. Eng. 80, 53–60.